Vortex flow generated by a magnetic stirrer

Gábor Halász, Balázs Gyüre, and Imre M. Jánosi[a)]
von Kármán Laboratory for Environmental Flows, Eötvös University, Pázmány P. s. 1/A,
H-1117 Budapest, Hungary

K. Gábor Szabó[b)]
Department of Fluid Mechanics, Budapest University of Technology and Economics, H-1111,
Bertalan L. u. 4-6, Budapest, Hungary

Tamás Tél
von Kármán Laboratory for Environmental Flows, Eötvös University, Pázmány P. s. 1/A,
H-1117 Budapest, Hungary

We investigate the flow generated by a magnetic stirrer in cylindrical containers by optical observations, particle image velocimetry measurements, and particle and dye tracking methods. The tangential flow is that of an ideal vortex outside a core, but inside downwelling occurs with a strong jet in the very middle. In the core region dye patterns remain visible over minutes indicating inefficient mixing in this region. The results of quantitative measurements can be described by simple relations that depend on the stirring bar's rotation frequency. The tangential flow is similar to that of large atmospheric vortices such as dust devils and tornadoes. © *2007 American Association of Physics Teachers.*

I. INTRODUCTION

Magnetic stirrers are commonly used in several types of laboratories to mix different materials dissolved in fluids. The main component is a magnet rotating with an adjustable frequency around a fixed vertical axis below a flat horizontal surface. The rotation of the magnet brings a magnetic stirrer bar into rotation on the bottom of a container placed on a flat surface. If the container is filled with a liquid, the bar generates fluid motion, which is believed to cause efficient stirring and mixing. A striking pattern of such flows is a big vortex above the stirrer bar and corresponding depletion, the funnel, on the surface (for a schematic see Fig. 1), which indicates that the flow is strongly structured.

Our goal is to investigate the fluid motion in cylindrical containers generated by magnetic stirrers. Despite the widespread use of this device, we could not find any reasonable description of such flows in the literature.

In the next section simple theoretical models of isolated vortices are reviewed. In Secs. III and IV we describe our experimental setup and method of data acquisition. In Sec. V we present the results of optical observations, of particle image velocimetry (PIV) measurements, and of monitoring tracer particles and dyes. Section VI is devoted to deriving simple relations for the vortex parameters based on the data. The concluding section discusses the similarities and the differences of our results compared to other whirling systems: Bathtub vortices, dust devils, and tornadoes.

II. THEORETICAL BACKGROUND

We review here the most important elementary models of steady isolated vortices in three-dimensional fluids of infinite extent.[1–3] Although our system is obviously more complicated then these models, they are useful for interpreting the data. The model flows are expressed in cylindrical (radial, tangential, and axial) velocity components (v_r, v_t, and v_z).

Rankine vortex. In this geometry the vorticity is uniformly distributed in a cylinder of radius c (in the notation of Ref. 3) with a central line (the z axis) as its axis. The tangential component is continuous in r but a break appears at c. The two other components vanish:

$$v_t = \begin{cases} \dfrac{Cr}{c^2} & (r \leq c) \\ \dfrac{C}{r} & (r > c), \end{cases} \tag{1}$$

with $v_r = 0$ and $v_z = 0$. Rigid body rotation takes place for $r < c$; outside a typical $1/r$-dependence appears with the parameter C proportional to the circulation of the flow. The limit $c \to 0$ corresponds to an ideal vortex line.

Burgers vortex. In a real fluid viscosity smooths out the break in the tangential component of the Rankine vortex. To maintain a steady rotation, an inflow and an axial flow should be present. In the Burgers vortex the strength of the axial flow increases linearly with the height z, measured from a certain level:
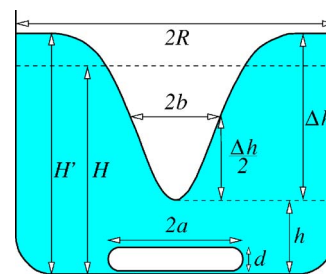

Fig. 1. The most important optically observable parameters of the system. The geometrical parameters are R, the radius of the cylinder, the half length a and the width d of the stirrer bar, and H, the height of the still water. While stirring, additional observable parameters are the displaced water height H', the distance h between the funnel's deepest point and the bottom of the container, the funnel's depth $\Delta h = H' - h$, and the halfwidth b.

Table I. The radii R of the cylinders used and the heights H of the water in each.

R (cm)	H (cm)
3.8	12.0
6.5	16.8
10.5	24.8
22.4	27.1

$$v_r = -\frac{2\nu}{c^2}r, \quad v_t = \frac{C}{r}(1 - e^{-r^2/c^2}), \quad v_z = \frac{4\nu}{c^2}z. \tag{2}$$

Here ν is the kinematic viscosity of the fluid, and c remains an effective radius within which the tangential flow is approximately a rigid body rotation. Note that the tangential velocity component may depend on the viscosity only indirectly via a possible ν dependence of the radius c.

III. EXPERIMENTAL SETUP

The experiments were carried out with tap water in glass cylinders of radius R and initial water height H as summarized in Table I. Two other relevant geometrical parameters are provided by the length $2a$ and the width d of the magnetic stirrer bars (see Fig. 1). The parameters of the bars used are summarized in Table II.

When the magnetic stirrer begins to rotate, the water column starts moving and after some time (which is on the order of minutes in our case) a statistically stationary flow sets in. Inherent fluctuations around the mean arise due to the periodic motion of the stirrer bar, the lack of a fixed axis of rotation, and turbulence. These are the reasons for the relative errors of our measurements being of the order of 10%. The most striking optically observable object is the funnel developing on the water surface. The height H' of the free surface at the perimeter and the characteristic sizes of the funnel, as defined in Fig. 1, can be easily measured (see Sec. IV).

IV. DATA ACQUISITION

The rotation frequency Ω of the stirring bar in the container with water was determined by means of a stroboscope whose frequency f is adjustable in a broad range. At certain frequencies f_n the bar appears to be at rest [see Fig. 2(a)], which occurs if the bar rotates at an integer multiple of half a period between two flashes:

$$\frac{\Omega}{f_n} = n\pi, \tag{3}$$

where n is an integer. The largest value of the f_ns uniquely determines the bar's rotation frequency as $\Omega = f_1\pi$. To reach

Table II. Parameters of the stirrer bars and the symbols used to denote the corresponding data in Figs. 3 and 9.

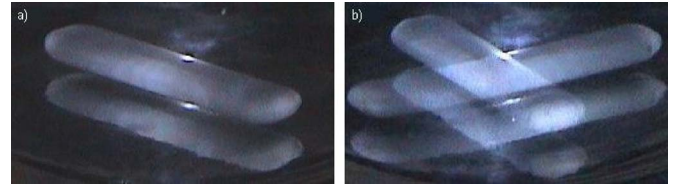| Stirrer bar	a (cm)	d (cm)	Symbol
1	2.05	0.85	$\triangledown$
2	2.50	0.90	$\square$
3	4.00	1.00	$\diamond$

Fig. 2. The picture of the bar (along with its mirrored image by the bottom) at stroboscopic frequencies (a) f_1 and (b) $f_{1/2}$.

a higher accuracy, we also determined the frequency $f_{1/2}$ when the bar rotates at a right angle between two flashes. This case is indicated by the appearance of a steady cross traced out by the bar on the bottom of the container [see Fig. 2(b)]. The bar's rotation frequency was determined as the average of the frequencies f_1 and $f_{1/2}$. The uncertainty in f is 0.1 Hz. In the range $\Omega = 20 – 120$ s^{-1} this uncertainty corresponds to a relative error of about 1%, which is negligible compared to the other errors.

The funnel parameters were determined via direct optical observations. The water height H' in the statistically stationary state was measured using a ruler. The depth of the funnel's deepest point can be determined in a similar way or by using a horizontal sheet of laser light (a laser beam opened by a cylindrical lens). From these two quantities, the funnel depth is $\Delta h = H' - h$ (see Fig. 1). The halfwidth of the funnel was measured on the back side of the cylinder. The length obtained this way was corrected by taking into account the optical effect caused by the cylindrical lens formed by the water column to obtain the value b. Both the funnel depth and width are subject to an error of about 10% due to fluctuations as discussed in Sec. III.

The PIV method was used to determine the velocity field in a plane defined by a horizontal laser sheet. From the positions of fine tracer particles on two subsequent images taken with a time difference of about 10^{-2} s, the displacement and velocity of the particles can be determined.[4] We used commercial PIV equipment (ILA GmbH, Germany) and determined the flow field in the largest container ($R = 22.4$ cm) at an intermediate water height ($H = 16.8$ cm) with stirrer bar 2 (see Table II) in different horizontal layers. The presence of the funnel and the strong downdraft make the PIV data unreliable in the middle of the container, within a region of radius of about 8 cm.

Particle tracking enables us to study the central region of the flow. We used plastic beads (low density polyethylene) of diameter ≈ 1 mm, which has a density of ≈ 0.92 g/cm^3. Despite being lighter than water, they sink below the funnel and often reach a dynamical steady state (for more detail see Sec. V C). The approximate strength of the downwelling in the middle was estimated from the rising velocity of the beads in a water column at rest. From several measurements in a separate narrow glass cylinder we found this rising velocity to be $7–8$ cm/s, for all the beads used.

The spreading of dye can provide a qualitative picture about the flow. A particularly important region is that around the axis of the vortex, where this coloring technique reveals fine details (see Sec. V D).

V. RESULTS

A. Frequency dependence of the funnel

The results of the optical observations of 16 cases (different containers, water heights, and stirring bars) each mea-
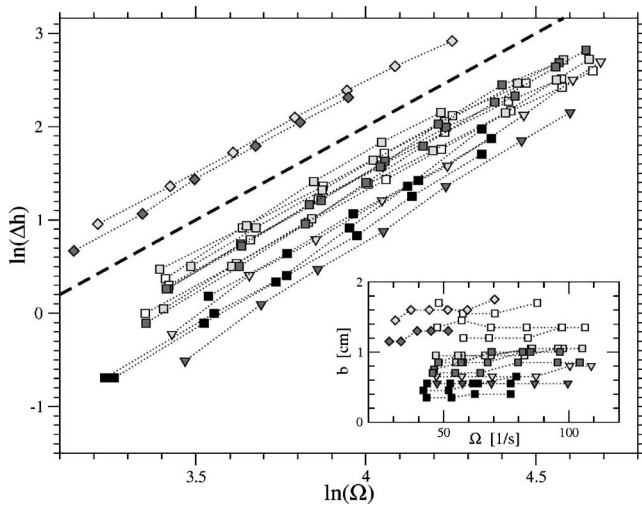
Fig. 3. Funnel depth as a function of the rotation frequency Ω in containers of different radii for different water heights and stirrer bars. The slope of the dashed line is 2. Inset: Funnel halfwidth as a function of Ω for several measurements. Different symbols mark different stirring bars (see Table II), and the level of grayness increases with the radius of the container. Symbols are not distinguished according to water heights.

sured at several frequencies Ω are summarized in Fig. 3. Although there is a clear frequency dependence on the funnel depth Δh, the halfwidth b appears to be independent of Ω (see inset) at least to the first approximation.

To extract the form of the frequency dependence, the funnel depth is plotted on a log-log scale in Fig. 3. The straight lines clearly indicate a power-law dependence given by

$$\Delta h \sim \Omega^2. \tag{4}$$

The coefficient (not given explicitly) depends more strongly on the stirring bar's parameters (a,d) than on the container's geometry (R,H).

B. Velocity fields

We present in Fig. 4 the result of a typical PIV measurement in a horizontal plane. The arrows mark velocity vectors. Arrows around the vortex center are considered to be unreliable because the vertical velocity components, not measurable by a planar PIV equipment used in the horizontal
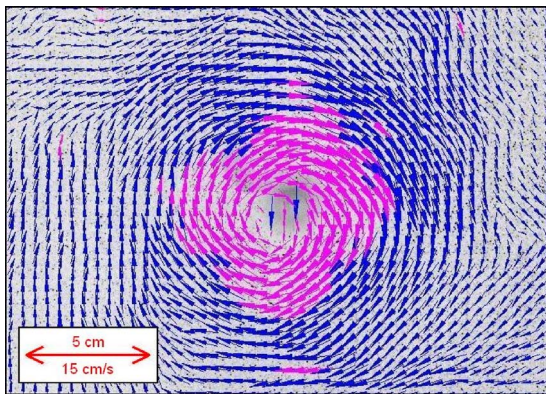

Fig. 4. Detail of a PIV image at the height $z=13$ cm taken at rotation frequency $\Omega=35.5$ s^{-1} ($R=22.4$ cm, $H=16.8$ cm, $a=2.5$ cm, $d=0.9$ cm). The inset sets the length and velocity scales.

plane, produce errors that are too large here. The flow is not fully axially symmetric as indicated by small secondary vortices, which appear around the edges of the picture.

To understand the mean flow, we divided each PIV image into narrow concentric rings and evaluated the average tangential and radial velocity in each band. These values were further averaged over several images taken at different times in the same flow and at the same height. In this way the effect of secondary vortices visible in Fig. 4 was averaged out. The procedure leads to a discrete representation of the functions $v_t(r)$ and $v_r(r)$. Both components appeared to be proportional to the frequency of the stirring bar. Therefore we present in Fig. 5 the components already divided by Ω. Because the results in the innermost region are not reliable, the components are displayed only for distances $r>8$ cm.

The measured tangential velocity data $v_t(r)$ can be approximated by the functional form A/r. This behavior is demonstrated by plotting the rescaled quantity $v_t r/\Omega$ in Fig. 5(a). (The multiplication by r magnifies the apparent error.) The coefficient A is a weakly decreasing function of the depth. Nevertheless, the tangential flow matches that of an ideal vortex to the first approximation. Accordingly, the vortex strength C is proportional to the frequency, that is,

$$C = A\Omega, \tag{5}$$

with a coefficient A extracted from the data to be $A=0.9\pm0.2$ cm^2.

In contrast to the tangential component, the radial component depends strongly on the height [Fig. 5(b)]. In the upper layers there is an inflow ($v_r<0$) for $r>8$ cm, which decays to zero as the height decreases. The level $z=4$ cm is dominated by outflow, but around $r=8$ cm a weak inflow survives.

The planar PIV algorithm does not provide any information on the vertical velocities. This component can, however, be determined from the continuity equation, which takes the form[1,3]

$$\frac{\partial v_z}{\partial z} = -\frac{1}{r}\frac{\partial(rv_r)}{\partial r} \tag{6}$$

in axisymmetric flows. We numerically integrated the left-hand side to obtain an approximation for $v_z(r)$ from the radial component. This component turns out to be also proportional to Ω. Qualitatively there is upwelling in the outermost region 4–5 cm and a slow downwelling in the intermediate region. The strong upwelling around the boundary of the container implies that there must be a strong downwelling in the very center, which cannot be resolved by means of the PIV method.

C. Particle tracking

The strength of downwelling at the very center of the vortex can be estimated by monitoring plastic beads, which float on the surface but eventually become trapped by the funnel. The beads slide down on the funnel surface and become advected downward toward the bulk of the fluid [see Fig. 6(a)]. Along the axis of the vortex the particles reach a dynamical steady state (with considerable fluctuations). This observation indicates that there is a strong downward jet in which the downward drag acting on the particle approximately compensates the upward resultant of gravity and buoyancy. As mentioned in Sec. IV, the asymptotic rising
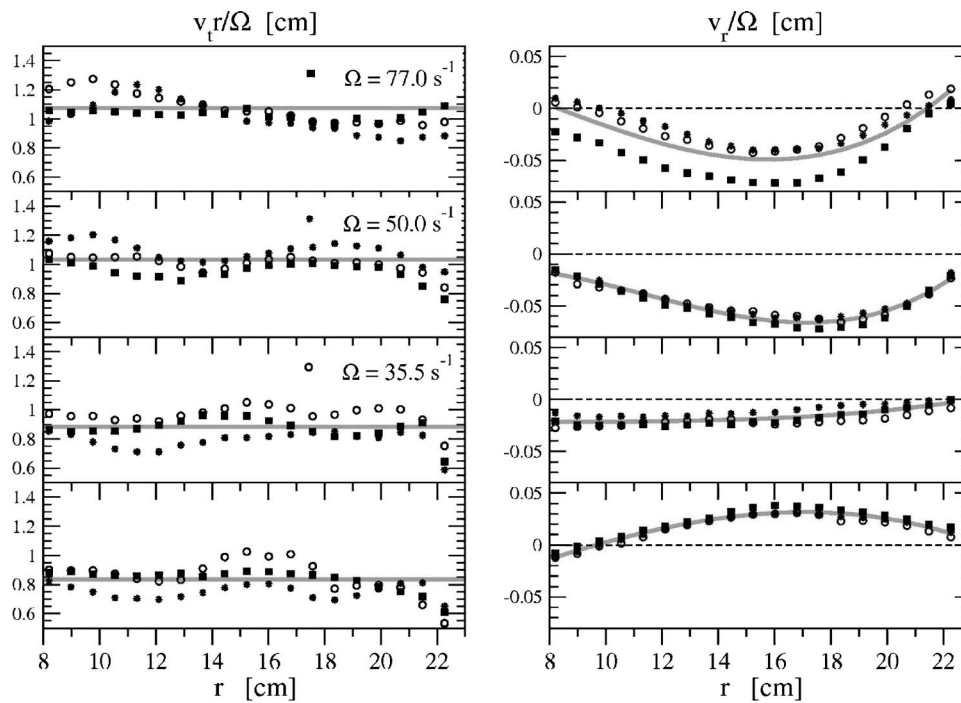
Fig. 5. (a) Rescaled tangential and (b) radial velocity components $v_t r/\Omega$ and v_r/Ω for three values of Ω (see legends). PIV measurements carried out at different heights $z = 16, 13, 8$, and 4 cm, from top to bottom. The horizontal lines in (a) are fitted average values. The smooth curves in (b) join the neighboring measured points to guide the eye.

velocity of the beads is $7-8$ cm/s in water at rest. Therefore we conclude that the strength of the downward jet is also $7-8$ cm/s.

A necessary condition for vertical stability is that the velocity of downwelling decreases when moving downward along the axis. Such a decrease is unavoidable in our case because the velocity should approach zero close to the lower bottom of the container. Experience shows that the average vertical position is shifted downward when the frequency Ω is increased, because this increase makes the jet somewhat stronger.

Stability is maintained in the horizontal direction as well due to the fact that in a rotating system an "anticentrifugal"
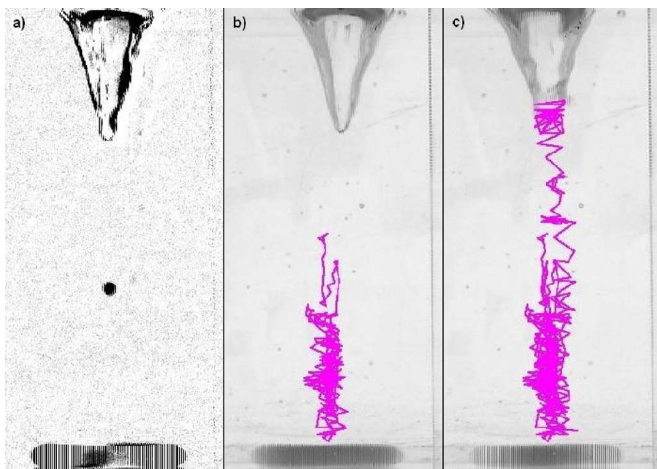

Fig. 6. Particle tracking. (a) A plastic bead lighter than water becomes washed downward below the funnel. (b) Path of the particle over 10 s. (c) Path of the particle over 20 s.

force acts on the beads because they are lighter than the surrounding fluid. Whenever a bead deviates from the axis, the "anticentrifugal" force directs it inward. This deviation is accompanied by an immediate rising of a bead, which indicates that the width of the strong downward jet is of the same order as the diameter of the beads. We conclude that this width is a few millimeters.

Due to the presence of all these effects and the permanent fluctuations of the flow, the overall motion of a bead is complex. After leaving the central jet, it starts rising but, due to the "anticentrifugal" effect we have mentioned, it is pushed back toward the center at a larger height. Then it is captured by the jet and starts moving downward again, and will leave the jet at a different level than previously. The bead remains within a cylindrical region around the vortex axis. We conclude that the bead motion is chaotic[5] [Fig. 6(b)]. By tracking a single bead over a long time interval, a chaotic attractor is traced [Fig. 6(c)].

D. Spreading of dye

When injecting dye into the water outside of the central region we observe the dye to spread very quickly. Very different behavior is found in the middle of the funnel. Very quickly, a cylindrical dye curtain develops around the vortex axis, which remains observable for about a minute (Fig. 7). This curtain can be seen at any value of the parameters (R, H, a, d, Ω) we investigated. The radius of the dye cylinder is of the order of the magnitude of the halfwidth $b = 1$ cm. It is remarkable that the wall of the cylindrical region containing the trapped beads coincides with this dye curtain [see Fig. 6(c)].

The existence of this long-lived dye curtain indicates that the radial velocity is approximately zero in a cylindrical an-
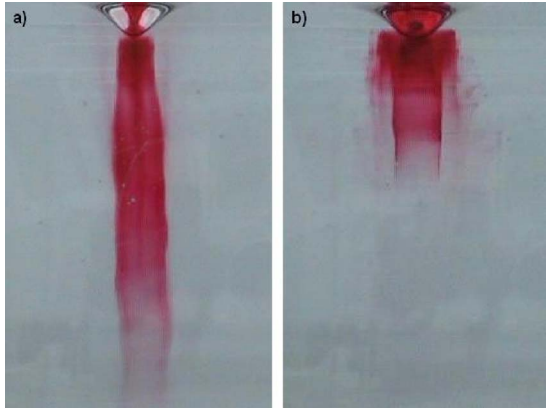
Fig. 7. (a) A stable cylindrical dye curtain (lifetime over a minute) develops below the funnel. (b) Sublayers can often also be observed.

nulus around the axis of rotation, the diameter of which is proportional to the width d of the stirring bar. Because a rotating bar continuously blocks the downward flow in a circle of diameter d, the suction is the strongest around the perimeter of this region. The downwelling has a maximum strength here and weakens inward. In the very center, there is the central jet mentioned in Sec. V C, and therefore the existence of a local minimum is necessary. The injected dye accumulates along the surface in which the downward velocity takes its local minimum. Thus both inside and outside the cylinder surface the downward flow is stronger than on the surface itself, where the injected dye accumulates. When injecting the dye somewhat off the cylinder we often observe more than one concentric curtain [see Fig. 7(b)], which indicates that there might be more local minima of the downward velocity in a region around the halfwidth of the funnel.

E. Qualitative picture

Based on the observations and the measurement of the velocity components, we obtain the following qualitative picture of the time averaged flow (see Fig. 8). In a given vertical slice two flow cells are formed by upwelling at the outer walls and downwelling in the middle. In three-dimensional space this pattern corresponds to a toroidal flow.
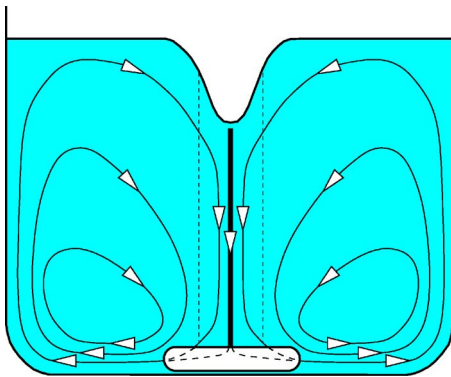

Fig. 8. Pattern of the time averaged flow. The thin continuous lines represent streamlines, the bold line denotes the downward jet, and the dashed line represents the average location of dye curtains.

The most striking feature is a strong downward jet in a very narrow filament on the axis of the vortex surrounded by a cylindrical region of weak downwelling.

VI. QUANTITATIVE RESULTS

A. Funnel depth

To obtain a simple expression for the funnel depth, we first apply dimensional analysis;[6–8] a comparison with the measured data then leads to a particular form. As dimensionless measures of the viscous and gravitational effects in the rotating flow, Reynolds and Froude numbers are introduced as

$$\text{Re} = \frac{\Omega a^2}{\nu} \quad \text{and} \quad \text{Fr} = \frac{\Omega a}{(gR)^{1/2}}\frac{d}{a}. \tag{7}$$

(The usual Froude number is multiplied by the factor d/a to simplify the following argument.) Small values of these numbers indicate strong viscous and gravitational effects. For our typical data ($\Omega = 50$ s^{-1}, $R = 10$ cm, $a = 2.5$ cm, $d = 1$ cm, $\nu = 10^{-2}$ cm^2 s^{-1}) we obtain Re$=3\times 10^4$ and Fr$=0.5$. These values indicate that gravity is essential, but viscosity is not so important for the overall flow. However, it is important on small scales such as near the center of the vortex.

The ratio $\Delta h/d$ must be a function of the dimensionless parameters. Therefore we can write

$$\frac{\Delta h}{d} = f\left(\text{Re}, \text{Fr}, \frac{a}{d}, \frac{a}{R}, \frac{H}{R}\right), \tag{8}$$

with f as an unknown function. Other dimensionless numbers might also be present. One candidate would be a measure of the surface tension. This effect we estimated in control experiments with surfactants, and found a negligible influence on our typical measurement error. Therefore, we do not include the corresponding dimensionless number in f.

If we assume that f is linear in both Re and Fr, we obtain

$$\frac{\Delta h}{d} = \text{Re Fr } \Phi\left(\frac{a}{d}, \frac{a}{R}, \frac{H}{R}\right). \tag{9}$$

This assumption is supported not only by Eq. (4), but also by other observations. A careful investigation of the data shows that the funnel depth is proportional to a^2, and for sufficiently large radii ($R > 0.4H$) it scales as $R^{-1/2}$. These observations imply

$$\frac{\Delta h}{d} = \frac{\Omega^2 a^2 d}{\nu (gR)^{1/2}} \Phi\left(\frac{H}{R}\right). \tag{10}$$

The form of the function $\Phi(x)$ can be estimated from a plot of the data as shown in Fig. 9. As the fitted smooth curve shows, a reasonable form for Φ is

$$\Phi(x) = \frac{1}{\alpha x + k}. \tag{11}$$

The best choices of the parameters are $\alpha = (0.58 \pm 0.08) \times 10^3$, $k = (2.8 \pm 0.2) \times 10^3$. The direct expression for the funnel depth is then

$$\Delta h = \frac{\Omega^2 a^2 d^2 R^{1/2}}{\nu(\alpha H + kR)g^{1/2}}. \tag{12}$$

The result shows that the dependence on the water height is rather weak, which explains why it was worthwhile to define the Froude number with R in Eq. (7). It is remarkable that
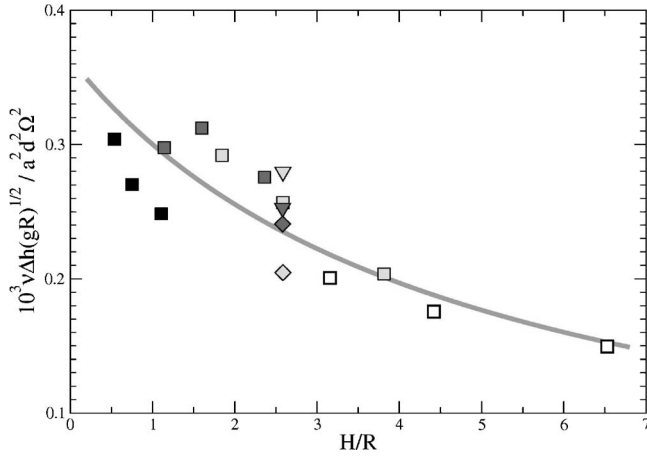
Fig. 9. The determination of the scaling function $\Phi(H/R)$ from the measured $\Delta h/\Omega^2$ values averaged over different Ω values. The continuous line is a fitted hyperbola of the form of Eq. (11). The fact that several measured values belong to a given H/R is due to the use of different stirrer bars. The symbols are the same as in Fig. 3.

such a simple relation fits the measured data with about 10% accuracy.

B. Halfwidth

The halfwidth b was found in Sec. V A to be independent of Ω. The ratio b/d can therefore be written as

$$\frac{b}{d} = \frac{\text{Fr}}{\text{Re}}\Psi\left(\frac{a}{d},\frac{a}{R},\frac{H}{R}\right) = \frac{d\nu}{a^2(gR)^{1/2}}\Psi\left(\frac{a}{d},\frac{a}{R},\frac{H}{R}\right). \quad (13)$$

The data provide an essentially H-independent halfwidth, which scales with $R^{-1/2}$. Therefore Ψ must be independent of H/R and a/R, that is,

$$\frac{b}{d} = \frac{d\nu}{a^2(gR)^{1/2}}\Psi\left(\frac{a}{d}\right). \quad (14)$$

Because the data show that b is approximately linearly proportional to a, the function $\Psi(x)$ should be cubic:

$$\Psi(x) = \beta x^3, \quad (15)$$

and the best fit yields $\beta = (2.8 \pm 0.8) \times 10^3$. The expression for the halfwidth is then

$$b = \frac{\beta a\nu}{d(gR)^{1/2}}. \quad (16)$$

Note that Eq. (16) does not contain the water height.

C. Interpretation in terms of a Burgers vortex

The fact that the rotating motion in the magnetic stirrer flow is accompanied by an inflow and a downwelling resembles the Burgers vortex described in Sec. II. Equation (2) defines the plane $z=0$ as a plane without vertical velocity. Because far away from the center there is no downwelling on the free surface at height H', the $z=0$ level should be chosen as the topmost level of the rotated water. The vortex model obtained in this way corresponds to the bulk of the investigated flow, far away from the external walls and the stirrer bar. It does not describe the upwelling near the walls or the outdraft around the stirring bar.

The time independent nature of the axisymmetric mean flow implies that the pressure gradient balances the centrifugal force and gravity in the radial and vertical direction:

$$\frac{\partial p}{\partial r} = \varrho\frac{v_t^2}{r}, \quad \frac{\partial p}{\partial z} = -\varrho g, \quad (17)$$

where ϱ is the fluid density. On the fluid's free surface at $z = \eta(r) < 0$, $d\eta/dr = -(\partial p/\partial r)/(\partial p/\partial z)$. Consequently,

$$\frac{d\eta}{dr} = \frac{v_t^2}{rg}. \quad (18)$$

By inserting the tangential velocity component from Eq. (2), the funnel depth can be obtained by integration:

$$\Delta h = \int_0^{R'} \frac{C^2}{r^3 g}(1 - e^{-r^2/c^2})^2 dr. \quad (19)$$

Here $R' \gg c$ is the radius within which the Burgers model is valid. Due to the exponential cutoff within the integrand, the integral can be well approximated by taking $R' = \infty$. We thus obtain

$$\Delta h = \ln 2\frac{C^2}{c^2 g}. \quad (20)$$

If we equate Eq. (20) with the funnel depth expression (12), we recover the relation $C = A\Omega$ found in Sec. V B with the coefficient

$$A = a^2\left(\frac{\beta^2\nu}{\ln 2(\alpha H + kR)(gR)^{1/2}}\right)^{1/2}. \quad (21)$$

Similarly, from $c \approx b$ and the halfwidth expression (16) based on the measured data, we obtain

$$c = \frac{\beta a\nu}{d(gR)^{1/2}}, \quad (22)$$

a relation used in Eq. (21). Thus we are able to express the parameters C and c of the Burgers vortex with the directly measurable parameters of the flow.

VII. DISCUSSION

We compare the fluid dynamical properties of our experiment with that of other whirling systems: Bathtub vortices, dust devils, and tornadoes. Detailed measurements of the velocities in these flows (see Refs. 9–12) indicate that, in spite of basic differences in the other components, the tangential component outside of the vortex core decays with the distance r as C/r, independently of height. The most dominant tangential component of all the flows is thus practically identical.

To estimate the degree of dynamical similarity in this component, we use another set of dimensionless numbers:

$$\text{Re}' = \frac{Uc}{\nu}, \quad \text{Fr}' = \frac{U}{(gH)^{1/2}}. \quad (23)$$

Here U represents the maximum velocity of the tangential flow component and c denotes the radius of the vortex core. The value of U can be estimated in our case to be a few tenths of m/s; we take $U = 50$ cm/s. The core radius and the height are $c \approx b \approx 1$ cm and $H \approx 20$ cm, respectively. The data for the other flows are taken from the literature[9–12] and

Table III. Parameters and dimensionless numbers for the tangential velocity components of the different types of flows.

Flow	U (m/s)	H (m)	c (m)	Re′	Fr′
Stirrer	0.5	0.2	10^{-2}	5×10^3	0.4
Bathtub	0.4	0.1	2×10^{-4}	8×10^2	0.4
Dust devil	25	10^3	50	8×10^7	0.25
Tornado	70	10^3	200	10^9	0.7

are summarized, along with the resulting dimensionless numbers in Table III.

The order of magnitude of all the Froude numbers is the same but the Reynolds numbers are rather different. This difference shows that the role of viscosity is much stronger in small scale flows then in the atmosphere. Viscous flow is present in the vortex core, and hence the detailed flow patterns do not match there. The global flow is in all cases practically that of an ideal fluid. Therefore we conclude that outside of the vortex core the tangential flows are dynamically similar, that is, our experiment faithfully models all these whirling systems, an observation that can be utilized in teaching.

Finally we mention that the analog of the dye curtain can be seen in tornadoes, typically in the vicinity of the bottom because it is the Earth's surface which is the source of "dye" (in the form of dust or debris). In some tornadoes this dye curtain is clearly separated from the funnel.[13]

ACKNOWLEDGMENTS

SUGGESTED PROBLEMS

Problem 1. Explore the advection properties of small objects of different sizes, shapes, and densities. Observe the rotation of elongated bodies (example, pieces of plastic straws) in the central jet. Their angular velocity monitors the local vorticity of the flow.

Problem 2. As mentioned, one source of experimental error is the oscillation of the stirrer bar. Try to eliminate this effect by slightly modifying the setup. Hint 1: Insert two magnetic stirrer bars in the opposite ends of a plastic tube with a hole between the two magnets. Use an external frame to fix a thin rod led through the hole to obtain a fixed axis of rotation. Hint 2: Use a narrow cylinder of nearly the same diameter as the length of the bar. Estimate the magnitude of the error and compare the parameters of the funnel in the modified and original setups.

[a] Author to whom correspondence should be addressed. Electronic mail: janosi@lecso.elte.edu

[b] Previous address: HAS Research Group for Theoretical Physics, H-1518, P.O. Box 32, Budapest, Hungary.

[1] L. D. Landau and E. M. Lifshitz, *Fluid Dynamics* (Pergamon, Oxford, 1987).

[2] H. J. Lugt, *Vortex Flow in Nature and Technology* (Wiley, New York, 1983).

[3] B. Lautrup, *Continuum Physics: Exotic and Everyday Phenomena in the Macroscopic World*, ⟨www.cns.gatech.edu/PHYS-4421/Whirls.ps⟩, Chap. 21.

[4] M. Raffael, C. E. Willert, and J. Kompenhans, *Particle Image Velocimetry: A Practical Guide* (Springer, Berlin, 1998).

[5] E. Ott, *Chaos in Dynamical Systems*, 2nd ed. (Cambridge U. P., Cambridge, 2002). T. Tél and M. Gruiz, *Chaotic Dynamics* (Cambridge U. P., Cambridge, 2006).

[6] P. K. Kundu, *Fluid Dynamics* (Academic, San Diego, 1990), Chap. 8.

[7] T. E. Faber, *Fluid Dynamics for Physicists* (Cambridge U. P., Cambridge, 1997), Sec. 1.5.

[8] Y. Nakayama and R. F. Boucher, *Introduction to Fluid Mechanics* (Arnold, London, 1999), Chap. 10.

[9] A. Andersen, T. Bohr, B. Stenum, J. J. Rasmussen, and B. Lautrup, "Anatomy of a bathtub vortex," Phys. Rev. Lett. **91**, 104502-1–4 (2003).

[10] R. Greeley, M. R. Balme, J. D. Iversen, S. Metzger, R. Mickelson, J. Phoreman, and B. White, "Martian dust devils: Laboratory simulation of particle threshold," J. Geophys. Res. **108**, 5041-1–5041-12 (2003).

[11] P. Sarkar, F. Haan, W. Gallus, Jr., K. Le, and J. Wurman, "Velocity measurements in a laboratory tornado simulator and their comparison with numerical and full-scale data," ⟨www.pwri.go.jp/eng/ujnr/joint/37/paper/42sarkar.pdf⟩.

[12] P. Sarkar and F. Haan, Jr., "Next generation wind tunnels for simulation of straight-line, thunderstorm- and tornado-like winds," ⟨www.pwri.go.jp/eng/ujnr/joint/34/paper/34sarkar.pdf⟩.

[13] See, for example, ⟨www.oklahomalightning.com⟩.